



Structured modulation multi-height microscopy for high-resolution imaging

LIMING YANG,^{1,2} YUJIN LEE,^{2,3} RUIHAI WANG,²
PENGMING SONG,² DIEGO ACKER CANDELA,⁴ TIANBO WANG,²
SHAOWEI JIANG,^{2,5} CHENGFEI GUO,² AND XIAOPENG SHAO^{1,*}

¹School of Optoelectronic Engineering, Xidian University, Xi'an 710071, China

²Department of Biomedical Engineering, University of Connecticut, Storrs, CT 06269, USA

³School of Electrical and Electronic Engineering, Yonsei University, Seoul 03722, Republic of Korea

⁴Hall High School, West Hartford, CT 06107, USA

⁵School of Communication Engineering, Hangzhou Dianzi University, Hangzhou 310018, China

*xphao@xidian.edu.cn

Abstract: Conventional multi-height microscopy techniques introduce different object-to-detector distances to obtain multiple measurements for phase retrieval. However, surpassing the diffraction limit imposed by the numerical aperture (NA) of the objective lens remains a challenging task. Here, we report a novel structured modulation multi-height microscopy technique for quantitative high-resolution imaging. In our platform, a thin diffuser is placed in between the sample and the objective lens. By translating the diffuser to different axial positions, a sequence of modulated intensity images is captured for reconstruction. The otherwise inaccessible high-resolution object information can thus be encoded into the optical system for detection. In the construction process, we report a ptychographic phase retrieval algorithm to recover the existing wavefront of the complex object. We validate our approach using a resolution target, a phase target, and various biological samples. We demonstrate a ~4-fold resolution gain over the diffraction limit. We also demonstrate our approach to achieve a 6.5 mm by 4.3 mm field of view and a half-pitch resolution of 1.2 μm . The reported methodology provides a portable, turnkey solution for quantitative high-resolution imaging with potential applications in disease diagnosis, sample screening, and other fields.

© 2023 Optica Publishing Group under the terms of the [Optica Open Access Publishing Agreement](#)

1. Introduction

Imaging biological samples often relies on fluorescent labels, which offer high contrast with molecular specificity. The use of exogenous labeling agents, however, may alter the normal physiology of the specimens. Quantitative phase imaging (QPI) [1] operates on unlabeled specimens and, as such, is complementary to established fluorescence microscopy. Phase information characterizes how much a light wave is delayed by propagation through a sample. However, conventional light detectors can only measure the intensity variations of incoming light waves, phase information is lost during the data acquisition, referred to as the “phase problem”. It was first noted in the field of crystallography [2], where the phase problem needs to be solved to determine the structure of a crystal from diffraction measurements. Phase retrieval is a valuable approach for recovering lost phase information from distinct intensity measurements. This technique involves reinforcing known intensities and allowing an initial phase “guess” to converge toward a solution that matches all measurements. To ensure robust phase retrieval, various types of diversity measurements are introduced, including defocus multiple-height diversity [3–7], multiple incident angles diversity [8–10], transverse translational diversity [11–13], multi-wavelength diversity [14–16], and nonlinear diversity [17] among others.

Defocus multi-height phase retrieval introduces different object-to-detector distances for phase diversity measurements. This concept was initially proposed for electron microscopy in 1968

[3]. In the optical region, it has been successfully demonstrated in wavefront reconstruction [4,5] and has shown great potential for lensless imaging in the visible light regime [6,14,15]. In a typical implementation of the conventional multi-height platform, the specimen is axially translated to different defocus distances for diffraction data acquisition. In the reconstruction process, the complex object solution is iteratively propagated to corresponding defocus planes, and the captured images are enforced as magnitude constraints. However, this approach still faces challenges related to the inherent trade-off between imaging resolution and field of view, imposing a limit on the system throughput [18–20]. One can have a large field of view with low-resolution or a small field of view with high-resolution, but not both [19,20]. As a result, preventing its widespread adoption in biomedical research, fall short for its low imaging throughput and limited resolution.

Here we report a novel coherent high-resolution imaging approach, termed structured modulation multi-height microscopy. In our platform, a thin diffuser is placed in between the sample and the objective lens, effectively modulating the complex light waves. The high-resolution object information, otherwise inaccessible, is now encoded in the captured images. By translating the diffuser to different axial positions, a sequence of modulated intensity images is captured. We then reconstruct the high-resolution exit wavefront of the complex object using a ptychographic phase retrieval process [12,13,21,22]. The remarkable aspect of our approach lies in the fact that the final achievable resolution is not determined by the NA of the objective lens. Instead, it is determined by the feature size of the diffuser. With simulation results, we demonstrate that as the feature size of the diffuser increases, there is a noticeable degradation of the reconstructed image. With experimental results, we demonstrate a ~4-fold resolution gain beyond the diffraction limit. We also demonstrate the reported platform to achieve a 6.5 mm by 4.3 mm field of view and a half-pitch resolution of 1.2 μm .

In contrast to coded-illumination high-resolution approaches [23–25], our platform offers a unique capability, image refocusing after data acquisition. Moreover, our reported approach models only the complex wavefront exiting the sample, rather than its entry, making the sample thickness inconsequential in the image formation process. Unlike coded-illumination approaches, including conventional ptychography and Fourier ptychography [26,27], which necessitate thin sample assumptions, our platform eliminates this constraint. After the reconstruction process, we can digitally propagate the complex wavefront back to any position along the optical axis. We conduct experimental validation of 3D digital refocusing capacity using a two-layer biological sample and a thick spider leg sample, which will be discussed in further detail later.

This paper is structured as follows: In Section 2, we will discuss the imaging model of the structured modulation multi-height imaging setup and propose a reconstruction scheme for recovering the complex object. We will also demonstrate the simulation results and show that different diffuser feature sizes will affect the reconstruction results. In Section 3, we will validate the effectiveness of the reported approach experimentally. Finally, we will summarize the results in Section 4.

2. Methods and simulations

2.1. Structured modulation multi-height setup

Figure 1 presents a comparison between the conventional multi-height platform and the proposed structured modulation multi-height platform. In the typical implementation of the defocus multi-height scheme (Fig. 1(a)), the sample is axially translated to different defocus positions for diffraction data acquisition. By capturing images of the sample at various heights under coherent illumination, this method holds significant potential for quantitative phase imaging. However, the achievable resolution is limited by the NA of the objective lens, posing challenges for further improvements. In contrast, the proposed platform (Fig. 1(b)), introduces a thin diffuser (coated $\sim 1 \mu\text{m}$ microspheres on a cover slip) between the sample and the objective lens. The

sample remains fixed, while the diffuser is translated to different axial positions, modulating the complex light waves. The diffuser can redirect the large angle diffracted waves into smaller angle for detection. Thus, otherwise inaccessible high-resolution details encoded in the captured images thereby substantially improves the resolution beyond the diffraction limit imposed by the objective lens.

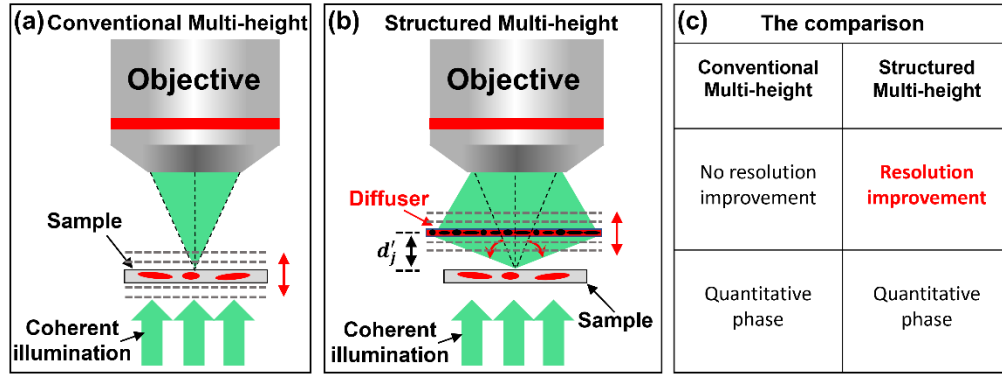


Fig. 1. Comparison between the conventional multi-height microscopy (a) and the proposed structured modulation multi-height microscopy (b). (c) The proposed method can achieve a resolution improvement.

2.2. Imaging model and reconstruction

The forward imaging model of the structured modulation multi-height approach in Fig. 1(b) can be described as follows: The incident plane waves first interact with the sample. The resulting complex wavefront of the object $W(x, y)$ propagates a distance d'_j to reach the diffuser layer. The exit light wave leaving the diffuser is given by the product of the diffuser profile $D(x, y)$ and the object wavefront after propagation. Finally, the modulated light wave is low pass filtered by the defocused coherent transfer function (CTF). Mathematically, this imaging model can be formulated as [13,28]:

$$I_j(x, y) = | W(x, y) * PSF_{free} \left(d'_j \right) \cdot D \left(x - x_j, y - y_j \right) * iFT \left\{ CTF_{d'_j} (k_x, k_y) \right\}^2 \quad (1)$$

where $I_j(x, y)$ represents the j th captured image by placing the diffuser at a distance of d'_j from the object. $W(x, y)$ represents the complex exit wavefront of the sample, $D(x, y)$ represents the complex profile of the diffuser, and (x_j, y_j) represents the transverse displacement errors generated during diffuser axial movement. $CTF_{d'_j}(k_x, k_y)$ represents the coherent transfer function with different defocus distance of $-d'_j$. $PSF_{free}(d)$ represents the convolution kernel for free-space propagation of distance d , “.” stands for point-wise multiplication, and “*” stands for convolution operation. iFT stands for inverse Fourier transform.

The reconstruction process of structured modulation multi-height approach aims to recover the complex wavefront of the sample $W(x, y)$, leveraging the captured images $I_j(x, y)$ with the diffuser translated to different axial positions (d'_j) s.

Before conducting the reconstruction process, we first need to recover the axial positional shifts of the diffuser d'_j . Figure 2 shows the workflow of the proposed axial positional shifts recovery method. To obtain the transmission profile of the diffuser, a calibration experiment was performed [29]. In this experiment, we selected an object devoid of slow-varying phase, typically a blood smear slide as the calibration object, and acquired ~ 1500 images by translating the diffuser to different lateral positions. These images assisted in the recovery of the diffuser profile using

the regularized ptychographical iterative engine (rPIE) [21,30]. We note that this calibration experiment only needs to be performed once. Once the diffuser profile is recovered, it becomes feasible to use it for subsequent experiments. The initial guess of the diffuser axial positions d_j is set to 4 μm (will be discussed in the next section). As depicted in Fig. 2, we obtain the low-resolution diffuser profile $D_j^{\text{low}}(x, y)$ in line 4. To estimate the transverse displacement errors generated during diffuser axial movement, cross-correlation analysis is performed in line 8. We then update the axial positional shifts of the diffuser by minimizing the image mean squared error (MSE) in line 11. This process is iteratively repeated with a smaller step size to achieve a refined axial positional shifts recovery. We experimentally verified the aforementioned method, as shown in the bottom of Fig. 2. The blue line represents the ground-truth positions, while the red line shows the finally recovered positional shifts after refinement. The agreement between recovered positional shifts and the ground truth validates the effectiveness of the proposed method.

Axial position estimation of the diffuser

Input: Raw image sequence I_j ($j = 1, 2, \dots, J$), the complex diffuser profile $D(x, y)$ and the initial guess of the axial position of the diffuser d_j

Output: the estimated axial position of the diffuser d'_j

```

1   for  $j = 1 : J$  (Different captured images by translating the diffuser along z axis)
2      $D^{\text{FT}}(k_x, k_y) = \text{FT}(D(x, y))$ 
3      $D_j^{\text{FT}}(k_x, k_y) = D^{\text{FT}}(k_x, k_y) \cdot CTF_{d_j}(k_x, k_y)$  % Defocused CTF corresponding to  $d_j$ 
4      $D_j^{\text{low}}(x, y) = \text{iFT}(D_j^{\text{FT}}(k_x, k_y))$ 
5     for  $z = -Z_1 : step_1 : Z_1$  (Parallel process with a large  $step_1$ )
6        $D_{j,z}^{\text{low}}(x, y) = D_j^{\text{low}}(x, y) * PSF_{\text{free}}(z)$  % Propagate the diffuser to different positions
7        $A_{j,z}(x, y) = |D_{j,z}^{\text{low}}(x, y)|^2$ 
8        $(x_{j,z}, y_{j,z}) = \arg \max_{(x_{j,z}, y_{j,z})} A_{j,z}(x, y) * I_j(x, y)$  % Cross-correlation
9        $A'_{j,z}(x, y) = A_{j,z}(x - x_{j,z}, y - y_{j,z})$ 
10    end
11     $d'_j = \arg \min_{d'_j} MSE(A'_{j,z}(x, y), I_j(x, y))$ 
12    Repeat step 2-11 with updated  $d'_j$  and a smaller  $step_2$ 
13  end

```

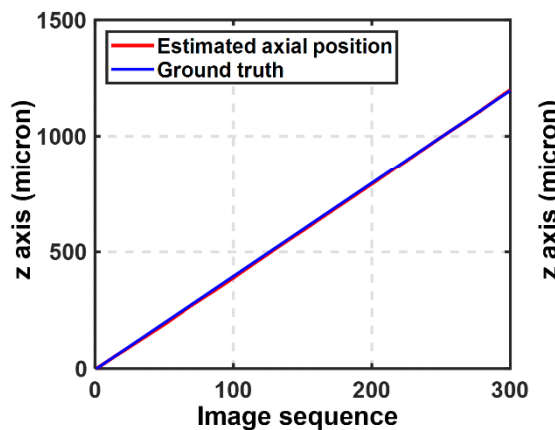


Fig. 2. The recovery process of axial position shifts of the diffuser.

The reconstruction process is shown in Fig. 3. We first initialize the amplitude of the object by averaging all measurements. We propagate the object to the diffuser plane with the estimated defocus distance of the diffuser d'_j and get the wavefront $W'_j(x, y)$ in line 4. We then multiply $W'_j(x, y)$ with the transversely position-corrected diffuser to obtain an exit wave $\phi_j(x, y)$ in line 6. The exit wave $\phi_j(x, y)$ is low pass filtered by the defocused CTF in the Fourier domain to get $\psi_j(x, y)$ in line 9. The defocused CTF is calculated based on the estimated d'_j . In line 10, the amplitude of $\psi_j(x, y)$ is replaced by the j th captured image. By using the rPIE algorithm, we update the Fourier spectrum of the exit wave $\phi_j(x, y)$ in the Fourier domain in line 11 [21]. Based on the updated exit wave $\phi'_j(x, y)$, we then update the object using rPIE algorithm in line 13 [30]. In line 14, the updated exit wave is propagated from the diffuser plane back to the object plane and gets the updated object wavefront. Steps 4-14 are repeated until a convergence condition is satisfied. Either a fixed number of iterations (in our implementation, the phase retrieval process converges within 15 iterations in all experiments) or stagnation of an error metric $E_N = \frac{\sum_j \sum_{x,y} |\sqrt{I_j(x,y)} - \psi_j(x,y)|^2}{\sum_j \sum_{x,y} I_j(x,y)}$ [21]. The process time for 300 raw images with 1024 pixels by 1024 pixels each is ~90 seconds for 15 iterations using a desktop computer with AMD Ryzen 5 5600X 6-Core 3.70 GHz processor.

Recovery process

Input: Raw image sequence I_j ($j = 1, 2, \dots, J$), the diffuser profile $D(x, y)$, the estimated defocus distance of the diffuser d'_j and the corresponding defocus CTF $CTF_{d'_j}$

Output: High-resolution exit wavefront $W(x, y)$

```

1 Initialize  $W(x, y)$ 
2 for  $n = 1 : N$  (Different iteration loops)
3   for  $j = 1 : J$  (Different captured images by scanning the diffuser along z axis)
4      $W'_j(x, y) = W(x, y) * PSF_{free}(d'_j)$  % Propagate the wavefront to the diffuser
5      $D_j(x, y) = D(x - x_j, y - y_j)$  % Lateral position correction
6      $\phi_j(x, y) = W'_j(x, y) \cdot D_j(x, y)$ 
7      $\Phi_j(k_x, k_y) = FT(\phi_j(x, y))$ 
8      $\Psi_j(k_x, k_y) = \Phi_j(k_x, k_y) \cdot CTF_{d'_j}(k_x, k_y)$ 
9      $\psi_j(x, y) = iFT(\Psi_j(k_x, k_y))$ 
10     $\Psi'_j(k_x, k_y) = FT(\psi_j(x, y) / |\psi_j(x, y)| \cdot \sqrt{I_j})$  % Amplitude replacement
11     $\Phi'_j = \Phi_j + \beta_\Phi \frac{conj(CTF_{d'_j})(\Psi'_j - \Psi_j)}{|CTF_{d'_j}|_{max}^2}$  % Update the spectrum
12     $\phi'_j(x, y) = iFT(\Phi'_j(k_x, k_y))$ 
13     $W'_{j, update} = W'_j + \frac{conj(D_{d'_j})(\phi'_j - \phi_j)}{(1 - \alpha_{obj})|D_{d'_j}|^2 + \alpha_{obj}|D_{d'_j}|_{max}^2}$  % Update the object
14     $W(x, y) = W'_{j, update} * PSF_{free}(-d'_j)$  % Propagate back to the object plane
15  end
16 end

```

Fig. 3. The reconstruction process of the proposed structured modulation multi-height approach.

2.3. Simulation

We assess the performance of the proposed approach with different diffuser feature sizes through simulation, as shown in Fig. 4. Figure 4(a) shows the input complex object. Figure 4(b1)-(e1) show the simulated diffuser profile with different feature sizes ('p', '2p', '3p' and '4p' respectively). Figure 4(b2)-(e2) show the simulated raw images through the diffuser with different feature sizes. In our simulation, the illumination wavelength is 532 nm, and the pixel size is 2.4 μm . Initially the diffuser-to-sample distance is 500 μm . By translating the diffuser to different axial positions with a step size of 4 μm to generate 300 raw images (all these parameters are selected based on our experimental setup). Following the reconstruction process outlined in Fig. 3, we successfully recover the complex wavefront of the object. The corresponding reconstruction results for different diffuser feature sizes are shown in Fig. 4(b3)-(e4). We quantify the reconstruction results using the structural similarity index measure (SSIM) between the recovered amplitude and the ground truth. It is evident that as the feature sizes of the diffuser increase, the quality of the reconstruction deteriorates, resulting in a decrease in the SSIM index. The reason can be explained as: the final NA of the proposed structured modulation multi-height approach is determined by the spatial frequency content of the diffuser profile added with the NA of the employed objective lens. The smaller the diffuser feature size, the higher the spatial frequency content of the diffuser profile, the higher resolution can be achieved.

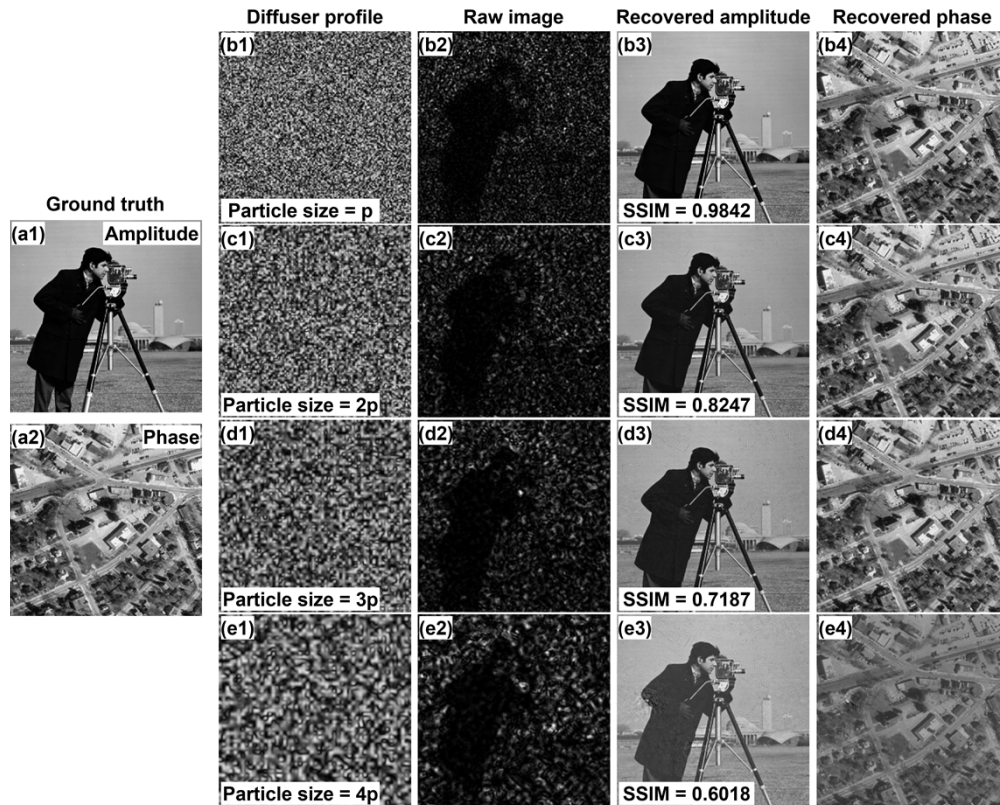


Fig. 4. The imaging performance with different diffuser feature sizes. (a1)-(a2) The input ground truth of amplitude and phase. (b1)-(e1) The simulated diffuser profile with different feature sizes. (b2)-(e2) Raw images corresponding to different diffuser feature sizes. (b3)-(e4) The recovered amplitude and phase of the object.

3. Experimental results

In our experiment setup, a fiber-coupled, 532-nm laser diode is used for sample illumination. A thin diffuser is placed between the sample and the objective lens for light wave modulation. At the detection path, image acquisition is performed using a microscope platform equipped with a low-NA objective lens ($2\times$, 0.065 NA) and a monochromatic image sensor (2.4 μm pixel size, Sony IMX 183CLK) with 20 frames per second and 1 ms exposure time. We use a mechanical stage (Applied Scientific Instrumentation LS50) to translate the diffuser along the axial direction. Initially, the distance between the diffuser and the sample is set to 500 μm . The speed of the stage is set to 80 μm per second, corresponding to a $\sim 4 \mu\text{m}$ distance between adjacent images. 300 raw images are captured in ~ 15 s, which are subsequently used for reconstruction.

3.1. Imaging performance characteristics

We evaluated and quantified the structured modulation multi-height approach using three types of objects: a resolution target (Fig. 5), a quantitative phase target (Fig. 6) and an unstained mouse kidney slide (Fig. 7).

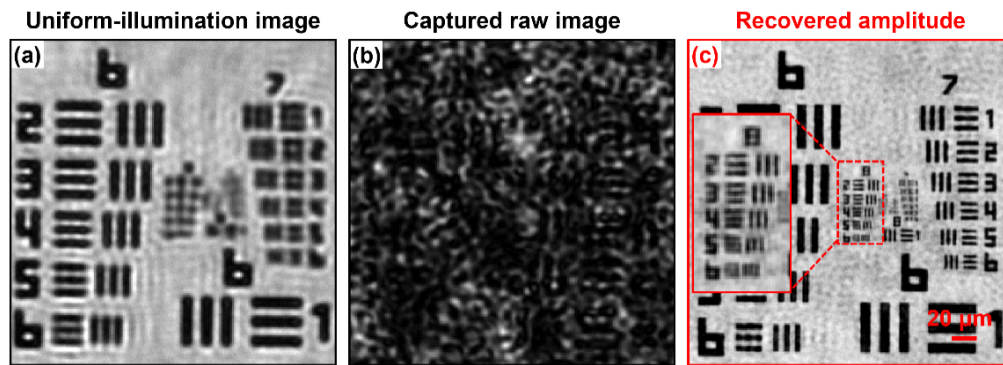


Fig. 5. Image quality quantification using a USAF resolution target. (a) The image under uniform illumination. (b) The captured raw image through the diffuser. (c) The recovered high-resolution amplitude image.

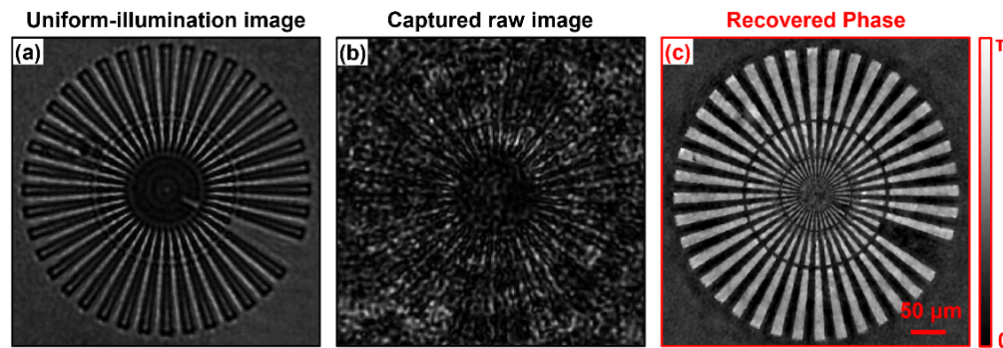


Fig. 6. Validating the quantitative imaging ability of the proposed approach using a quantitative phase target. (a) The image under uniform illumination. (b) The captured raw image through the diffuser. (c) The recovered phase image.

Figure 5(a) shows the captured image of a USAF resolution target under uniform-illumination and that the diffraction-limited resolution is 4.38- μm half-pitch linewidth, corresponding to group

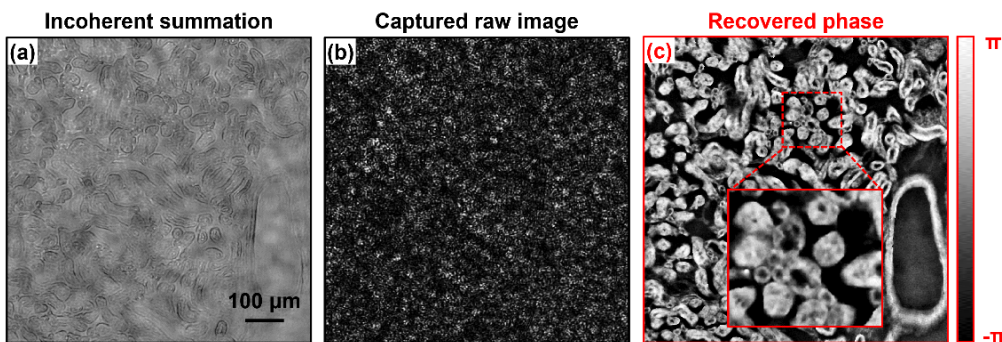


Fig. 7. Test on an unstained mouse kidney slide. (a) The incoherent summation of all captured images. (b) The captured raw image through the diffuser. (c) The recovered phase image.

6, element 6. Figure 5(b) shows the captured raw image, where the speckle feature comes from the diffuser modulation. Figure 5(c) shows our high-resolution recovery of the resolution target, where we can resolve 1.23- μm linewidth of group 8, element 5 on the resolution target. Achieving a ~4-fold resolution gain over the limit of the employed objective lens. The final NA of the proposed platform is determined by both the spatial frequency content of the diffuser profile and the NA of the employed objective lens. The current achievable resolution is limited by the feature size (~1 μm) of the diffuser. One can use smaller particles to further improve the modulation capability.

In the next experiment, we validate the quantitative imaging capability of the proposed approach. We image a quantitative phase target (Benchmark QPT). Figure 6(a)-6(c) exhibit the captured image under uniform illumination, the captured raw image with diffuser modulation and the recovered quantitative phase, respectively. The diffuser layer plays a crucial role in both intensity and phase modulation, contributing to the successful high-resolution quantitative phase imaging.

We then present an expanded evaluation of the structured modulation multi-height approach by imaging an unstained mouse kidney slide. Figure 7(a) shows the incoherent summation of all captured images. Figure 7(b) and 7(c) show the captured raw image and the recovered quantitative phase image of the mouse kidney slide, respectively. From the zoomed-in view of one highlighted region in Fig. 7(c), the detailed features of mouse kidney can be clearly observed, demonstrating the utility of the quantitative phase map in visualizing the otherwise transparent structure of the specimens. The quantitative phase imaging capability of the reported approach offers a label-free solution for cell-assay-related applications. This feature provides a powerful tool for studying biological samples without the need for staining or labeling, enabling noninvasive and high-resolution investigations of cellular structures and behaviors.

3.2. Imaging thick biological samples

The proposed platform is its ability to perform diffuser modulation at the detection path. This feature eliminates the need to model the complex wavefront entering the sample, a constraint present in other methods like FPM and other illumination-based spatial domain ptychography, particularly when dealing with thicker samples. Consequently, the sample thickness becomes irrelevant during reconstruction process. After recovery, we can propagate the complex wavefront to any position along the axial direction. To validate this capability, we conducted the following two experiments. For the first experiment, we image a two-layer biological sample consisting of two pathology sections separated by two coverslips, as shown in Fig. 8. Figure 8(a) and 8(b) show

the captured raw image and the recovered amplitude of the object exit wavefront, respectively. Figure 8(c1) and 8(c2) show the recovered object amplitude after digitally propagating to different axial planes, specifically at $z = 210 \mu\text{m}$ and $z = 1010 \mu\text{m}$. Figure 8(c1) brings the top layer into focus, while Fig. 8(c2) shifts the focus to the bottom layer.

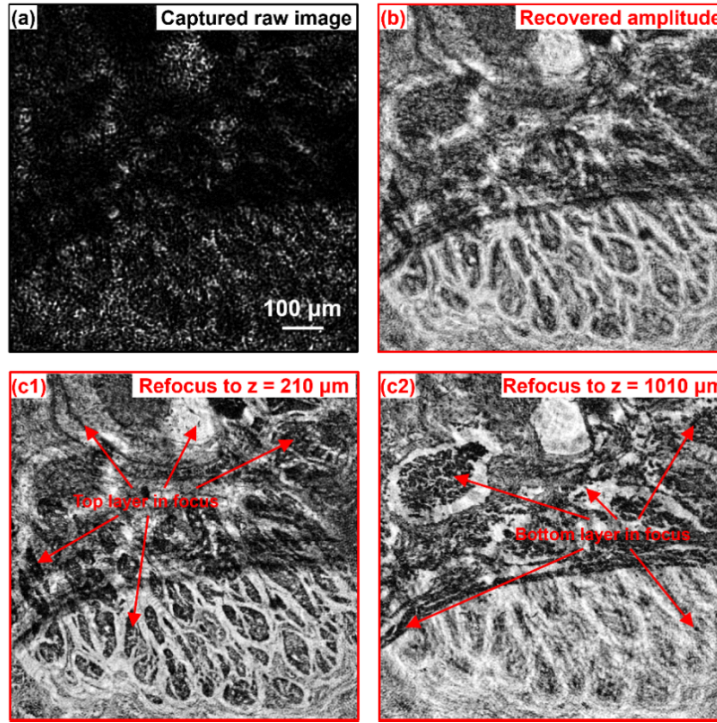


Fig. 8. Validation of the reported approach using a two-layer sample. (a) The captured raw image through diffuser. (b) The recovered amplitude of the two-layer object. Digital propagation of the recovered complex wavefront to the top layer (c1) and bottom layer (c2) ([Visualization 1](#)).

In the second experiment, we image a thick spider leg. Figure 9(a) shows the recovered amplitude of the object exit wavefront. Figure 9(b)-(d) show the recovered amplitude after digitally propagating to $z = 160 \mu\text{m}$, $z = 650 \mu\text{m}$, and $z = 1100 \mu\text{m}$, respectively.

For a more detailed visualization of the digital propagating process of the recovered wavefront, please refer to [Visualization 1](#) and [Visualization 2](#).

3.3. Imaging *in-vitro* yeast culture

In Fig. 10, we demonstrate the application of our platform using an *in vitro* yeast culture. To prepare the yeast, we are inoculating 2 ml of yeast extract peptone dextrose (YPD) medium with a yeast colony isolated from a fresh YPD agar plate. The culture was then incubated overnight at 30°C with 150 rpm. On the following day, we prepared a fresh 1 ml YPD culture by inoculating 1 ml of YPD with 0.1 ml of the overnight culture. This fresh culture was incubated with gentle agitation for 1 hour at 30°C . To culture the yeast on glass slides, we created a thin YPD solid agar layer on top of a cover glass. Next, we add a 20 μl aliquot of the yeast suspension onto the YPD agar layer. The yeast culture on the cover glass was then incubated at 30°C for 8 hours, allowing the yeast to grow and develop. After the incubation period, we placed the yeast culture slide in our structured modulation multi-height microscopy platform for image acquisition. Figure 10(a)

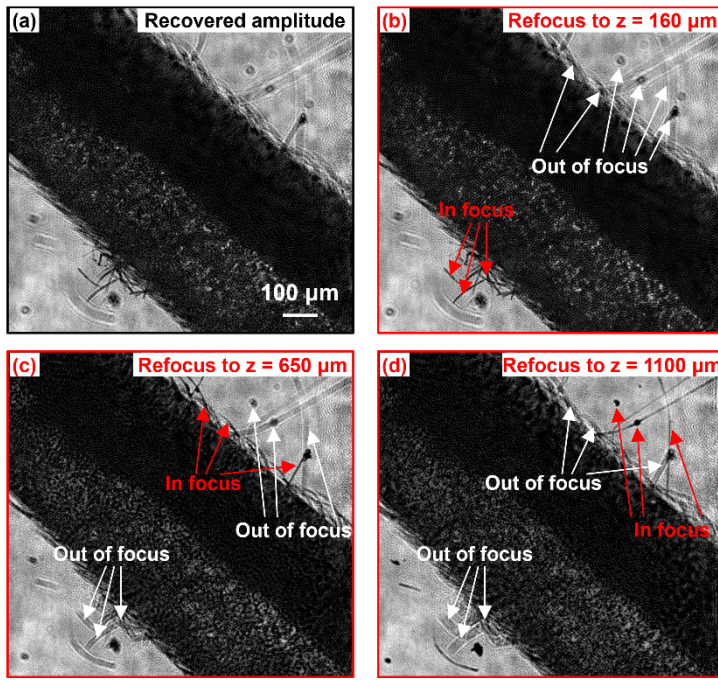


Fig. 9. Validation of the reported approach using a thick spider leg. (a) The recovered amplitude. (b)-(d) Three images after digitally propagating to three different axial positions (Visualization 2).

shows the captured image of the yeast culture under uniform-illumination. Figures 10(b) and 10(c) show the captured raw image and the recovered phase image, respectively. The results demonstrate the effectiveness of our approach in imaging yeast cultures, providing valuable insights into their structure and behavior.

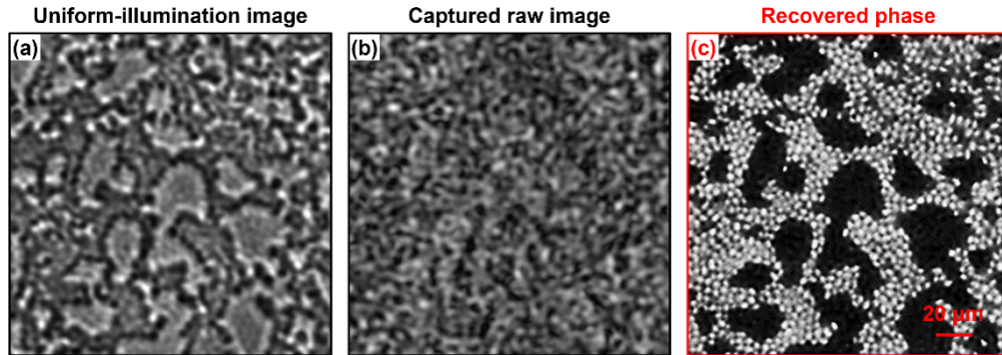


Fig. 10. Test for *in-vitro* yeast cell imaging. (a) The image under uniform illumination. (b) The captured raw image through the diffuser. (c) The recovered phase image.

3.4. High-resolution imaging over a large field of view

In microscopy imaging, the pursuit of achieving both high-resolution and a large field of view is highly desirable for various biomedical applications, such as digital pathology and haematology.

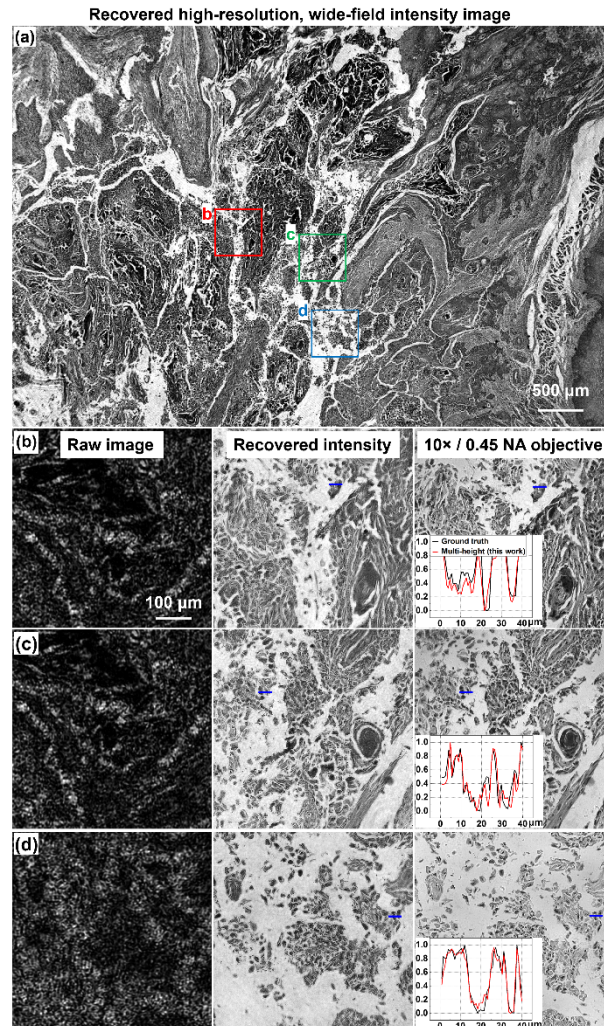


Fig. 11. High-resolution, wide-field imaging of a stained esophagus cancer slide. (a) The full field of view of the recovered object intensity. (b)-(d) Raw images, recovered intensity images (first two columns) and ground-truth images captured using a 10 \times , 0.45 NA objective lens (final column) of the three highlighted regions in Fig. 11(a).

However, conventional lens-based multi-height microscopy has a limited space-bandwidth product that restricts its ability to deliver both high-resolution and a large field of view. Our structured modulation multi-height platform offers a solution to this constraint, allowing us to benefit from the best of both worlds. We validate the high-resolution over a large field of view using a stained esophagus cancer slide, as shown in Fig. 11. Figure 11(a) shows the recovered high-resolution, large field of view intensity image of the stained esophagus cancer slide with a 6.5 mm by 4.3 mm field of view. Three zoomed-in views of Fig. 11(a) are presented in Fig. 11(c)-11(d). The captured raw images and the recovered intensity images are shown in the first two columns, respectively. We can clearly resolve the cellular structures within the sample from the recovered amplitude images. For comparison, the final column shows the ground-truth images captured using a 10 \times , 0.45 NA objective lens, along with an inset illustrating the line trace of the region marked by the blue straight line. The congruent trends between the proposed approach (red curves) and the

ground truth (black curves) validate the effectiveness of the proposed approach. The proposed structured modulation multi-height microscopy successfully overcomes the trade-off between resolution and field of view commonly encountered in conventional multi-height microscopy.

4. Conclusion

In summary, we present the design and implementation of a structured modulation multi-height platform for quantitative high-resolution microscopy. Our platform overcomes the trade-off between spatial resolution and imaging field of view, as well as the constraints in spatial resolution, field of view, and imaging throughput typically associated with conventional multi-height microscopy. Our experimental results demonstrate the proposed approach achieves a ~4-fold resolution gain beyond the diffraction limit. We also demonstrate our approach to achieve a 6.5 mm by 4.3 mm field of view and a half-pitch resolution of 1.2 μm .

Additionally, another advantage of our platform is its ability to modulate the light wave at the detection path, thus, the recovered image relies solely on the complex wavefront exiting the object. This removes the need for the thin object assumption, which has constrained conventional ptychography and FPM. By eliminating this constraint, our platform offers greater flexibility, particularly when working with thicker specimens. This attribute expands the scope of applications for our platform.

Finally, the true quantitative contrast of the complex object provided by our approach is of immense value, particularly in the context of point-of-care and telemedicine applications. The ability to precisely quantify and analyze complex structures and interactions within biomedical samples opens up new horizons for diagnostics and research. We anticipate further advancements and applications of this technique, as it holds promise across numerous biomedical domains.

Funding. China Scholarship Council (202006960022); National Natural Science Foundation of China (61975254, 62075175).

Disclosures. The authors declare no conflicts of interest.

Data availability. Data underlying the results presented in this paper are not publicly available at this time but may be obtained from the authors upon reasonable request.

References

1. G. Popescu, *Quantitative phase imaging of cells and tissues* (McGraw-Hill Education, 2011).
2. D. Sayre, "Some implications of a theorem due to Shannon," *Acta Crystallogr.* **5**(6), 843 (1952).
3. P. Schiske, "Image reconstruction by means of focus series," in *Proceedings of the 4th European Conference on Electron Microscopy, Rome, Italy, 1968*, (Tipografia poliglotta, 1968).
4. Y. Zhang, G. Pedrini, and W. Osten, *et al.*, "Whole optical wave field reconstruction from double or multi in-line holograms by phase retrieval algorithm," *Opt. Express* **11**(24), 3234–3241 (2003).
5. B. H. Dean and C. W. Bowers, "Diversity selection for phase-diverse phase retrieval," *J. Opt. Soc. Am. A* **20**(8), 1490–1504 (2003).
6. A. Greenbaum and A. Ozcan, "Maskless imaging of dense samples using pixel super-resolution based multi-height lensfree on-chip microscopy," *Opt. Express* **20**(3), 3129–3143 (2012).
7. A. Greenbaum, Y. Zhang, and A. Feizi, *et al.*, "Wide-field computational imaging of pathology slides using lens-free on-chip microscopy," *Sci. Transl. Med.* **6**(267), 175 (2014).
8. W. Luo, A. Greenbaum, and Y. Zhang, *et al.*, "Synthetic aperture-based on-chip microscopy," *Light: Sci. Appl.* **4**(3), e261 (2015).
9. Z. Zhang, Y. Zhou, and S. Jiang, *et al.*, "Invited Article: Mask-modulated lensless imaging with multi-angle illuminations," *APL Photonics* **3**(6), 060803 (2018).
10. P. Li and A. Maiden, "Lensless LED matrix ptychographic microscope: problems and solutions," *Appl. Opt.* **57**(8), 1800–1806 (2018).
11. H. M. L. Faulkner and J. Rodenburg, "Movable aperture lensless transmission microscopy: a novel phase retrieval algorithm," *Phys. Rev. Lett.* **93**(2), 023903 (2004).
12. M. Guizar-Sicairos and J. R. Fienup, "Phase retrieval with transverse translation diversity: a nonlinear optimization approach," *Opt. Express* **16**(10), 7264–7278 (2008).
13. S. Jiang, J. Zhu, and P. Song, *et al.*, "Wide-field, high-resolution lensless on-chip microscopy via near-field blind ptychographic modulation," *Lab Chip* **20**(6), 1058–1065 (2020).

14. P. Bao, F. Zhang, and G. Pedrini, *et al.*, “Phase retrieval using multiple illumination wavelengths,” *Opt. Lett.* **33**(4), 309–311 (2008).
15. W. Luo, Y. Zhang, and A. Feizi, *et al.*, “Pixel super-resolution using wavelength scanning,” *Light: Sci. Appl.* **5**(4), e16060 (2016).
16. X. Wu, J. Sun, and J. Zhang, *et al.*, “Wavelength-scanning lensfree on-chip microscopy for wide-field pixel-super-resolved quantitative phase imaging,” *Opt. Lett.* **46**(9), 2023–2026 (2021).
17. C.-H. Lu, C. Barsi, and M. O. Williams, *et al.*, “Phase retrieval using nonlinear diversity,” *Appl. Opt.* **52**(10), D92–D96 (2013).
18. A. W. Lohmann, R. G. Dorsch, and D. Mendlovic, *et al.*, “Space-bandwidth product of optical signals and systems,” *J. Opt. Soc. Am. A* **13**(3), 470–473 (1996).
19. J. Park, D. J. Brady, and G. Zheng, *et al.*, “Review of bio-optical imaging systems with a high space-bandwidth product,” *Adv. Photonics* **3**(04), 044001 (2021).
20. G. Zheng, C. Shen, and S. Jiang, *et al.*, “Concept, implementations and applications of Fourier ptychography,” *Nat. Rev. Phys.* **3**(3), 207–223 (2021).
21. A. M. Maiden and J. M. Rodenburg, “An improved ptychographical phase retrieval algorithm for diffractive imaging,” *Ultramicroscopy* **109**(10), 1256–1262 (2009).
22. S. Jiang, P. Song, and T. Wang, *et al.*, “Spatial- and Fourier-domain ptychography for high-throughput bio-imaging,” *Nature protocols* **18**, in press (2023).
23. H. Zhang, Z. Bian, and S. Jiang, *et al.*, “Field-portable quantitative lensless microscopy based on translated speckle illumination and sub-sampled ptychographic phase retrieval,” *Opt. Lett.* **44**(8), 1976–1979 (2019).
24. M. Stockmar, P. Cloetens, and I. Zanette, *et al.*, “Near-field ptychography: phase retrieval for inline holography using a structured illumination,” *Sci. Rep.* **3**(1), 1–6 (2013).
25. H. Zhang, S. Jiang, and J. Liao, *et al.*, “Near-field Fourier ptychography: super-resolution phase retrieval via speckle illumination,” *Opt. Express* **27**(5), 7498–7512 (2019).
26. P. Thibault, M. Dierolf, and A. Menzel, *et al.*, “High-resolution scanning x-ray diffraction microscopy,” *Science* **321**(5887), 379–382 (2008).
27. G. Zheng, R. Horstmeyer, and C. Yang, “Wide-field, high-resolution Fourier ptychographic microscopy,” *Nat. Photonics* **7**(9), 739–745 (2013).
28. T. Wang, S. Jiang, and P. Song, *et al.*, “Optical ptychography for biomedical imaging: recent progress and future directions,” *Biomed. Opt. Express* **14**(2), 489–532 (2023).
29. S. Jiang, P. Song, and T. Wang, *et al.*, “Spatial- and Fourier-domain ptychography for high-throughput bio-imaging,” *Nat. Protoc.* **18**(7), 2051–2083 (2023).
30. A. Maiden, D. Johnson, and P. Li, “Further improvements to the ptychographical iterative engine,” *Optica* **4**(7), 736–745 (2017).